Geometrical analysis of the refraction and segmentation of normal faults in periodically layered sequences

Martin P.J. Schöpfer [a,*], Conrad Childs [a], John J. Walsh [a],
Tom Manzocchi [a], Hemin A. Koyi [b]

[a] *Fault Analysis Group, School of Geological Sciences, University College Dublin, Belfield, Dublin 4, Ireland*
[b] *Hans Ramberg Tectonic Laboratory, Department of Earth Sciences, Uppsala University, Villavägen 16, SE-752 36 Uppsala, Sweden*

Abstract

Normal faults contained in multilayers are often characterised by dip refraction, which is generally attributed to differences in the mechanical properties of the layers, sometimes leading to different modes of fracture. Because existing theoretical and numerical schemes are not yet capable of predicting the 3D geometries of normal faults through inclined multilayer sequences, a simple geometric model is developed, which predicts that such faults should show either strike refraction or fault segmentation, or both. From a purely geometrical point of view, a continuous refracting normal fault will exhibit strike (i.e. map view) refraction in different lithologies if the intersection lineation of fault and bedding is inclined. An alternative outcome of dip refraction in inclined multilayers is the formation of segmented faults exhibiting en échelon geometry. The degree of fault segmentation should increase with increasing dip of bedding, and a higher degree of segmentation is expected in less abundant lithologies. Strike changes and associated fault segmentation predicted by our geometrical model are tested using experimental analogue modelling. The modelling reveals that normal faults refracting from pure dip-slip predefined faults into an overlying (sand) cover will, as predicted, exhibit systematically stepping segments if the base of the cover is inclined.
© 2006 Elsevier Ltd. All rights reserved.

Keywords: Fault geometry; Fault refraction; Fault segmentation; En échelon; Sandbox modelling

1. Introduction

Normal faults contained in multilayer sequences show a range of geometrical complexities arising from propagation-related phenomena (Fig. 1). For example, fault traces observed in cross section are often refracted with steeply dipping segments in the strong layers and shallow dipping segments in the weak ones (Wallace, 1861; Dunham, 1948, 1988; Ramsay and Huber, 1987; Peacock and Zhang, 1993; Mandl, 2000; Sibson, 2000; Ferrill and Morris, 2003; Fig. 1b). Fault refraction, referred to as 'steep and flat structure' in Ramsay and Huber (1987, p. 518), has been variously attributed to either different modes of fracturing (e.g.

Ferrill and Morris, 2003) or to different friction coefficients within the interbedded lithologies (e.g. Mandl, 2000). A difference in the mode of fracture within individual layers typically occurs at low effective stress, where one lithology (the 'strong' one) has a strength that facilitates failure in tension, whereas the other lithology (the 'weak' one) fails in shear (Schöpfer et al., 2006). Another propagation-related characteristic of normal faults is that they often display segmentation in 3D (Ramsay and Huber, 1987; Peacock and Sanderson, 1994; Childs et al., 1995, 1996; Walsh et al., 1999, 2003), providing fault segment traces that step laterally in plan view (Segall and Pollard, 1980; Peacock and Sanderson, 1991, 1994; Childs et al., 1995). If the stepping of fault segments or fractures is systematic, the resulting geometry is commonly referred to as en échelon. Stepping faults can either overlap or underlap and the distance between the tips of the two faults measured parallel to the segments is the

---

* Corresponding author. Tel.: +353 1 7162611; fax: +353 1 7162607.
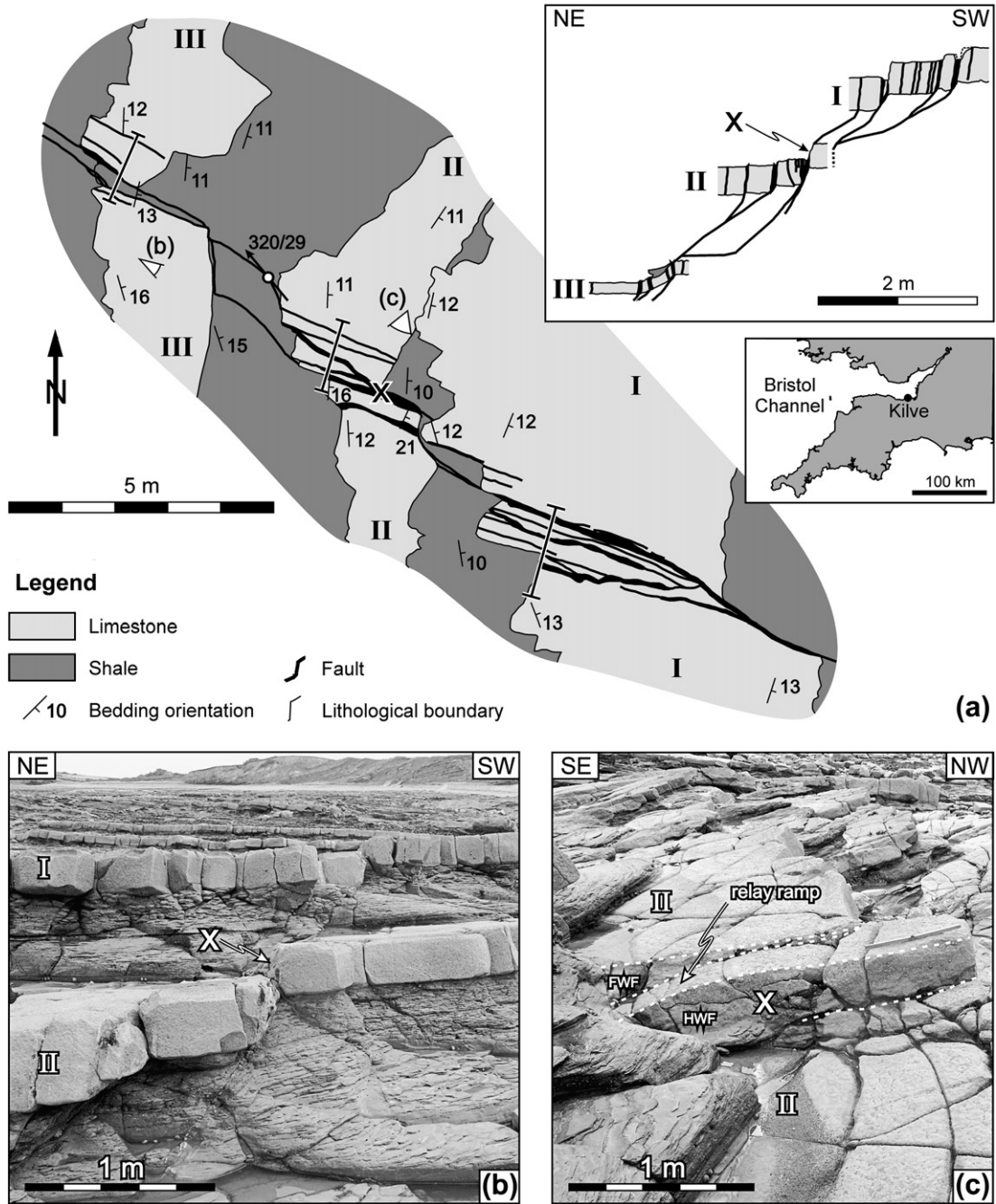 *E-mail address:* martin@fag.ucd.ie (M.P.J. Schöpfer).

Fig. 1. Natural example of a refracted and segmented sinistral oblique-slip normal fault. (a) Map and cross section of fault zone located NE of Quantock's Head (ST 13786 44559; see inset for location map), Kilve foreshore, Somerset, UK. Fault throw decreases from 40 cm in the SE to 25 cm in the NW. The fault is highly segmented both laterally (in map view) and vertically (viewed in cross sections). White dot with arrow is slickenside lineation. Both the limestone and shale layers are laterally continuous with constant thickness; discontinuous layer map patterns are due to staircase-like erosion. Also note that the mapped area has significant topography, which generates an apparent right-stepping of the faults from one limestone bed to the other. The systematic stepping referred to in the text is observed within each limestone bed. The map was drawn at a scale of 1:100, whereas the cross sections were constructed at a scale of 1:50; the sections are therefore slightly more detailed than the map. The cross section shown is not a vertical slice through the fault zone, but a composite of three individual sections, which are highlighted in the map as H-bars. (b,c) Photos of mapped fault zone. Standpoint and field of view of photos are shown on the map. (b) Strike parallel photo of fault zone taken standing on layer III, with limestone layer II in the foreground and layer I in the background. Notice fault refraction. (c) Oblique photo of layer II showing a relay ramp between two right-stepping fault segments within the limestone layer. FWF and HWF denote footwall and hangingwall fault, respectively. In all diagrams fault segment X is labelled for clarity.

overlap (or underlap) length. Increased displacement on overlapping segments leads to the steepening of intervening relay ramps and eventually to the formation of fault-bound lenses (e.g. Larsen, 1988; Peacock and Sanderson, 1991; Walsh et al., 1999; Imber et al., 2004; Fig. 1c). Despite the importance of fault refraction and segmentation in the growth of fault zones, very few mechanical/numerical models incorporate both processes (Mandl, 2000).

When a fault propagates through a rock volume it rarely does so as a single planar surface but as an irregular and, to a greater or lesser extent, segmented array of faults. Segmentation is due to local retardation or acceleration of propagation of the fault tip-line, controlled by the heterogeneous nature of the rock volume (e.g. Jackson, 1987); heterogeneities occur on a range of scales, from grain-scale to crustal scale. A fundamental question regarding the propagation of faults is, under which states of stress or strain is a fault expected to be (systematically) segmented? One way of addressing this question was proposed by Mandl (1987; revisited by Treagus and Lisle, 1997) who showed that Coulomb−Mohr shear failure planes will be discontinuous within homogeneous, isotropic volumes if continuous $\sigma_I \sigma_{II}$-principal planes of stress cannot be defined. Mandl's method (1987), however, has not yet been developed into a scheme for predicting the detailed 3D geometry of segmentation within a multilayer sequence. Another approach is to investigate the 3D state of stress or strain in two different materials that are separated by a coherent interface (Treagus, 1981, 1983, 1988; Goguel, 1982; Mandl, 2000). These studies have shown that under many circumstances (e.g. when none of the principal axes of stress or strain are contained within the interface, or when a shear couple is applied to two layers with different initial differential stress) principal planes of stress or strain will be discontinuous across the interface. As Treagus (1988) points out, it is, however, difficult to justify the application of this approach to faulting within multilayers because it requires the unlikely scenario that the onset of faulting occurs simultaneously in the two materials (Treagus, 1988; Mandl, 2000).

In this paper we use an alternative approach, which is non-mechanical and based purely on geometry, to investigate the circumstances in which faults are expected to be segmented within dipping multilayer sequences. Our simple geometric model of normal faults suggests that fault segmentation and/or map view (i.e. strike) refraction are inevitable consequences of fault dip refraction within dipping multilayer sequences. The basic characteristics of this model are illustrated using a simple stereonet construction showing that a continuous normal fault that refracts across an inclined bedding plane will also refract in map view if the strike of bedding and the fault are not the same (Fig. 2). In these circumstances, strike refraction arises because the fault/bedding intersection lines are different for different layers (Fig. 2a); this does not occur when the fault and bedding have the same strike. Although combined dip and strike refraction provides a means of generating a continuous fault, it requires different amounts of oblique-slip motion over different parts of the continuous fault surface (Figs. 2b and 3b). An alternative outcome, which does not require oblique-slip motion, is that the geometrical complications arising from differing fault/bedding intersection lines for different layers are accommodated by the localisation of segmented dip-slip fault arrays (Fig. 3c), where the degree of segmentation depends on the relative geometries of fault and bedding; for the purposes of this paper, the degree of segmentation is the number of segments per unit length along a segmented fault array. This geometrical model provides
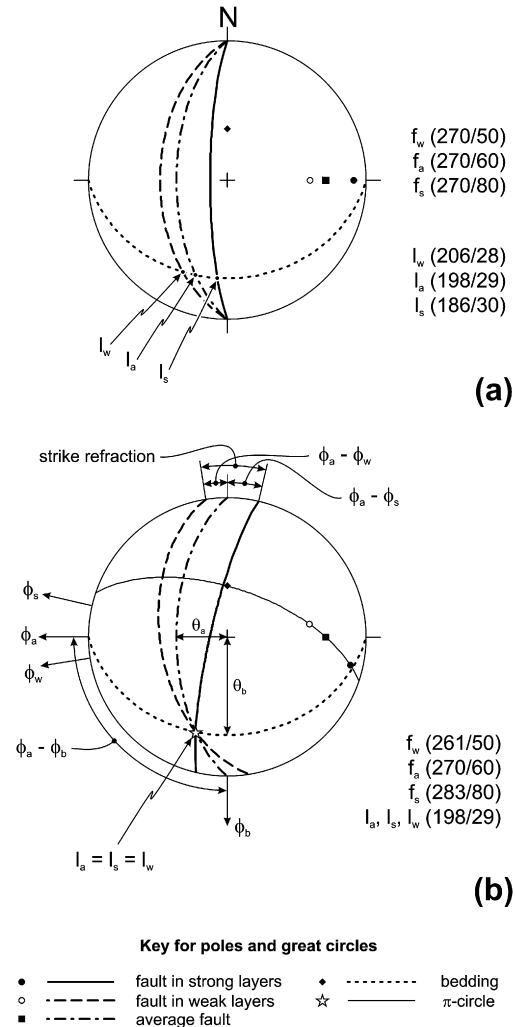

Fig. 2. Lower hemisphere, equal area stereographic projections illustrating the problem of continuous refracting faults. Fault orientations are given as dip direction (ϕ) and dip (θ). Bedding is oriented (180/30) and the average fault is oriented (270/60). The symbols and parameters used in this study are shown and summarized in Table 1. In (a) the intersection lineations of the fault in strong (l_s) and weak (l_w) layers and the average fault (l_a) with bedding are given and labelled in the stereonet. Since the intersection lines are not parallel to each other a continuous refracting fault cannot exist: a continuous fault surface demands that the intersections with bedding are the same. In (b) the dip directions of the fault in the strong and weak layers were rotated in order to obtain a continuous refracting fault plane. Consequently the intersection lineations of the fault with bedding are parallel to each other.

a means of estimating the geometry and degree of fault segmentation, an approach that is tested using a series of plane strain physical models of faulting within a cover sequence above an underlying predefined fault with an inclined intersection with the base−cover interface. The experimental modelling results verify our geometrical approach and demonstrate, for example, that systematic stepping of fault segments in the cover above a reactivated basement fault is not necessarily a kinematic indicator for oblique-slip reactivation. We then show how our simple model offers one plausible mechanism for generating highly segmented fault arrays including that shown in Fig. 1. We suggest that a continuous (non-segmented) fault in a multilayer may be the exception rather

No fault refraction
bedding (180/45)
f_a (270/59)

N

dip direction, ϕ_a

dip, θ_a

difference in dip
direction between
fault and bedding, ϕ_a - ϕ_b

(a)

Continuous refracting fault
f_s (292/80)
f_w (255/50)

N

apparent dip of fault
in strong layer, θ'_s

apparent dip of fault
in weak layer, θ'_w

strike changes

strong

weak

(b)

Discontinuous refracting fault
f_s (270/79)
f_w(255/50)

N

ϕ_a

θ_a

$\phi_{en\ èchelon} = \phi_a$

$\theta_{en\ èchelon} = \theta'_s$

strong

weak

average fault strike =
strike of en échelon segments

(c)

Key for poles and great circles

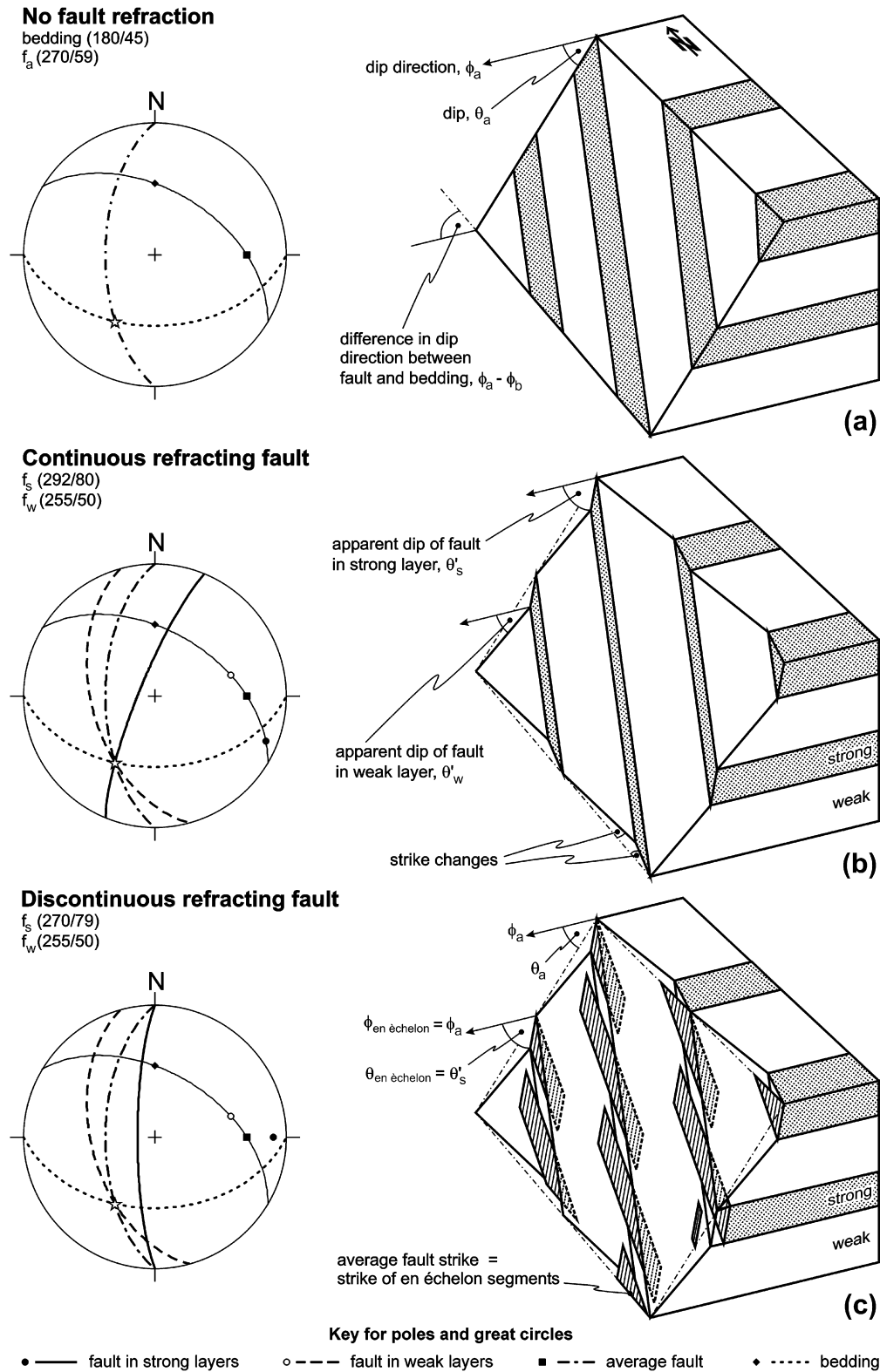●—— fault in strong layers   ○ – – – fault in weak layers   ■ –·– average fault   ◆ ····· bedding

Fig. 3. Stereographic projections and block diagrams illustrating the normal fault geometries discussed and analysed in this study. Bedding orientation (180/45), the average fault orientation (270/59) and the thickness ratio ($t_s/t_w =$ 0.6) are the same in all diagrams. Measured parameters are shown in Fig. 2 and a list of symbols is given in Table 1. (a) Planar normal fault (i.e. with no dip or strike refraction) offsetting inclined bedding, for which the fault-bedding intersections for different layers are parallel to each other. (b) Continuous refracting fault, a geometry that demands a difference in fault strike between different layers. The absolute strike change is greater in the less abundant layers (strong — stippled) than in the more abundant layers (weak — unornamented) and the change in dip direction is clockwise in the former and anti-clockwise in the latter. (c) Block diagram of a segmented fault. For the sake of clarity segmentation is only shown for faults contained in the strong (stippled) layers. The en échelon segments have the same dip direction as the average fault. The dip of the segments is the apparent dip (measured in a cross section normal to the strike of the average fault) of a median plane passing through the en échelon arrays. The fault segments are layer-bound, right-stepping and pure dip-slip (slickensides are schematically indicated). The tip lines of individual segments are shown, for simplicity, as rectangular although in reality elliptical tip lines are perhaps more likely. If the fault contained in the weak layers were discontinuous rather than continuous, the layer-bound dip-slip en échelon segments would be left-stepping.

than the rule and that lithological/mechanical stratigraphy is extremely important for understanding the segmented nature of faults. This study focuses on normal fault geometries within gently dipping beds for two reasons: (i) the geometry of normal faults within horizontal to gently dipping layering is better defined than for normal faults within steeply dipping beds; and (ii) dramatic fault dip variation (refraction) often requires that layers fail in different modes (extension vs. shear failure), which is promoted at low effective stress and therefore more likely in extensional settings (e.g. Sibson, 1998). Nevertheless, our approach and general findings could be applicable to any type of fault showing fault refraction within multilayer sequences.

2. Introduction to the geometrical analysis

The aim of this paper is to describe methods for evaluating the likely impact of differences in fault dip in different lithologies on fault surface geometry. The purely geometrical approach adopted in this study requires only a few known parameters, which can be quite often estimated for natural systems. The parameters include (i) the dips of normal faults in the two different lithologies comprising the periodically layered sequence, (ii) the thickness ratio of the two lithologies, which is the thickness of the strong layers divided by the thickness of the weak layers in the periodically layered sequence, and (iii) the orientation of bedding relative to the 'average' fault plane (which is taken to be parallel to the enveloping surfaces of a refracting fault). Fig. 3 introduces the geometries that will be discussed in detail in the following two sections and Fig. 2 illustrates some of the geometrical parameters discussed. A list of symbols is given in Table 1. Fig. 3a shows a block diagram and the stereonet solution for a planar (i.e. non-refracting) normal fault in a dipping sequence. Fig. 3b shows the same sequence with a normal fault exhibiting refraction. The refracted nature of the fault plane when combined with bedding that has a different dip direction leads to a situation in which fault-bedding intersections within each lithology are different, with neither being parallel to the intersection of bedding and the 'average' fault plane through the multilayer (Fig. 2a). This geometric problem could be solved by generating a continuous fault plane, but this requires

Table 1
List of symbols

ϕ	Dip direction
θ	Dip angle
θ'	Apparent dip angle
t	Layer thickness
ψ	Strike difference between fault segments and fault array
L	Fault segment length
O	Fault overlap length
S	Fault separation
T	Fault throw

Subscripts 's' and 'w' in this paper refer to faults contained in the 'strong' and 'weak' layers, respectively. Other subscripts used are 'a' for average fault and 'b' for bedding.
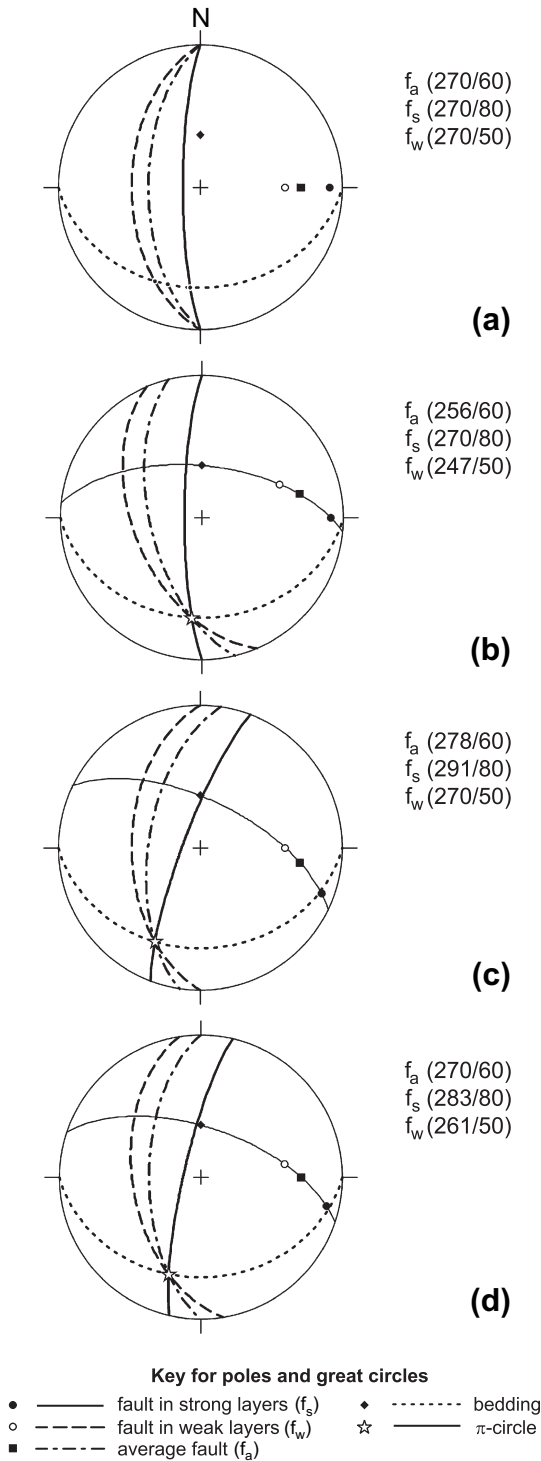
different fault dip directions and differing departures from pure dip-slip motion in the two lithologies (Figs. 2b and 3b). In Section 3, we consider some of the geometrical implications of this continuous fault model, which is one end-member geometry considered in this study. Fig. 3c shows another quite different solution to the geometrical problem, with the fault localising first in the strong layers as an array of en échelon segments, each of which is dip-slip and has the same dip direction as the 'average' fault. This model does not involve geometries that demand strike changes and associated oblique-slip motion, but does require fault segmentation, which is in fact a relatively common phenomenon associated with faults. This model, which is our favoured solution to the geometrical issues confronted by fault growth through dipping multilayers, is the other end-member geometry considered in this study, and is described in more detail in Section 4.

3. Continuous refracting faults

3.1. Geometry

For the geometrical model of a continuous refracting fault (Fig. 3b) we make the following assumptions: (i) fault dips in the individual lithologies comprising the multilayer are constant irrespective of their strike or the orientation of layering; (ii) the multilayer sequence is periodically layered and consists of two materials that exhibit different fault dips; (iii) layers containing steep and shallow dipping faults are taken to be "strong" and "weak", respectively, an assumption that is true in many if not all circumstances. The block diagram shown in Fig. 3b illustrates the 3D geometry of a continuous refracting fault. The fault trace refracts both in cross section and in map view. The geometry of this fault can be obtained using a stereonet or numerically.

3.2. Stereonet solution

Consider a refracting normal fault in a periodically layered sequence consisting of two different materials. The fault dips in the strong and weak material are θ_s and θ_w, respectively, and the average fault dip, θ_a, is somewhere in-between. Bedding is not necessarily horizontal and need not have the same dip direction as the fault. The thickness ratio, t_s/t_w, of the two materials is a variable which can either be prescribed or derived (see below). A simple stereonet construction (Fig. 4a) reveals that when the bedding dip direction is oblique to the fault dip direction, formation of a continuous refracting fault surface, which refracts at the bedding plane, is complicated by the fact that the fault planes in the two materials do not share the same intersection lineation with the bedding plane.

In order to obtain a continuous surface, the dip direction in one of the two materials could be changed (Fig. 4b and c). However, this leads to a change of the average dip direction. A continuous refracting fault therefore demands a change of dip direction of the faults contained in both materials (Fig. 4d). The intersection lineation of the fault planes in the two materials with the bedding plane is the same and

f_a (270/60)
f_s (270/80)
f_w (270/50)

(a)

f_a (256/60)
f_s (270/80)
f_w (247/50)

(b)

f_a (278/60)
f_s (291/80)
f_w (270/50)

(c)

f_a (270/60)
f_s (283/80)
f_w (261/50)

(d)

Key for poles and great circles

- ● ——— fault in strong layers (f_s)
- ○ – – – fault in weak layers (f_w)
- ■ –·–·– average fault (f_a)
- ◆ ········ bedding
- ☆ ——— π-circle

Fig. 4. Lower hemisphere, equal area stereographic projections illustrating the problem of continuous refracting faults. Fault orientations are given as (dip direction/dip). Bedding is oriented (180/30) and the average fault dip is 60° in all plots. In (a) a continuous fault plane does not exist, since the intersections of the fault planes and the bedding plane do not coincide. In (b) the strike of the shallow dipping fault is adjusted in order to form a continuous plane. This, however, leads to anti-clockwise rotation of the average fault plane. In (c) the strike of the steeply dipping fault is adjusted, which results in a clockwise rotation of the average fault plane. In (d) the strikes of both the shallow and steeply dipping fault are adjusted to provide a continuous refracting fault contained within a multilayer with a thickness ratio, t_s/t_w, of 1.4, which was calculated using Eq. (1).

contained within the average fault plane. The intersection lineation of the average fault with the bedding plane is defined as the pole to a great circle that, in the case of a continuous fault, contains the poles of the faults in the strong and weak layers. This great circle could be called the fault π-circle, in accordance with the nomenclature used for cylindrical folds. In the example shown in Fig. 4d, the fault in the strong layers (f_s) is rotated clockwise relative to the average fault (f_a) whereas the fault in the weak layers (f_w) is rotated anti-clockwise. The average fault dip (θ_a) is a function of (i) the fault dips in the strong and weak layers, (ii) the orientation of bedding (ϕ_b and θ_b) relative to the orientation of the average fault, and (iii) the thickness ratio of the two materials, t_s/t_w. Measured in a vertical section perpendicular to the strike of the average fault the following relationship, which is derived in Appendix A, is obtained:

$$\frac{t_s}{t_w} = \left[\frac{\tan(\theta_a - \theta_b')}{\tan(\theta_w' - \theta_b')} - 1\right]\left[1 - \frac{\tan(\theta_a - \theta_b')}{\tan(\theta_s' - \theta_b')}\right]^{-1} \tag{1}$$

where the apparent dips (primed values) are measured in this section. Hence, for predefined fault dips in the strong and weak layers and a predefined dip of the average fault, the thickness ratio can be obtained using the stereonet and Eq. (1). Alternatively, the same geometric problem can be solved numerically for predefined fault dips in the strong and weak layers and for a predefined thickness ratio.

3.3. Numerical solution, maps and cross sections

In the following analysis[1] the parameters are (i) the fault dips in the strong and weak layers, θ_s and θ_w, respectively, (ii) the average fault dip direction, ϕ_a, and (iii) the thickness ratio, t_s/t_w. The orientation of bedding (ϕ_b and θ_b) is varied systematically and the dip directions of the fault in the strong and weak layers (ϕ_s and ϕ_w) respectively, and the average fault dip (θ_a), are obtained from Eq. (1) by converging to the solution using the bisection method. In order to illustrate the geometries clearly we chose a thickness ratio of 1.0 and fault dips in the strong and weak layers of 80° and 50°, respectively. These dip values and a fault refraction of 30° are typical for normal faults in limestone/mudrock sequences where faulting occurred under low effective stress (Peacock and Zhang, 1993; fig. 4). A sensitivity study where we varied the thickness ratio and the fault dips in the strong and weak layers is given later in this section.

Contour plots of strike refraction, i.e. the change in strike from one lithology to the other, and the average fault dip as a function of dip of bedding and difference in dip direction between the average fault and bedding are shown in Fig. 5. These plots reveal that, if bedding is dipping and has a different strike to the average fault, strike refraction occurs and the

---

[1] A MATLAB® script for obtaining the geometry of a continuous refracting fault in a periodically layered sequence is available upon request from the corresponding author.

strike refraction

(a)

$t_s/t_w = 1$
$\theta_s = 80°$
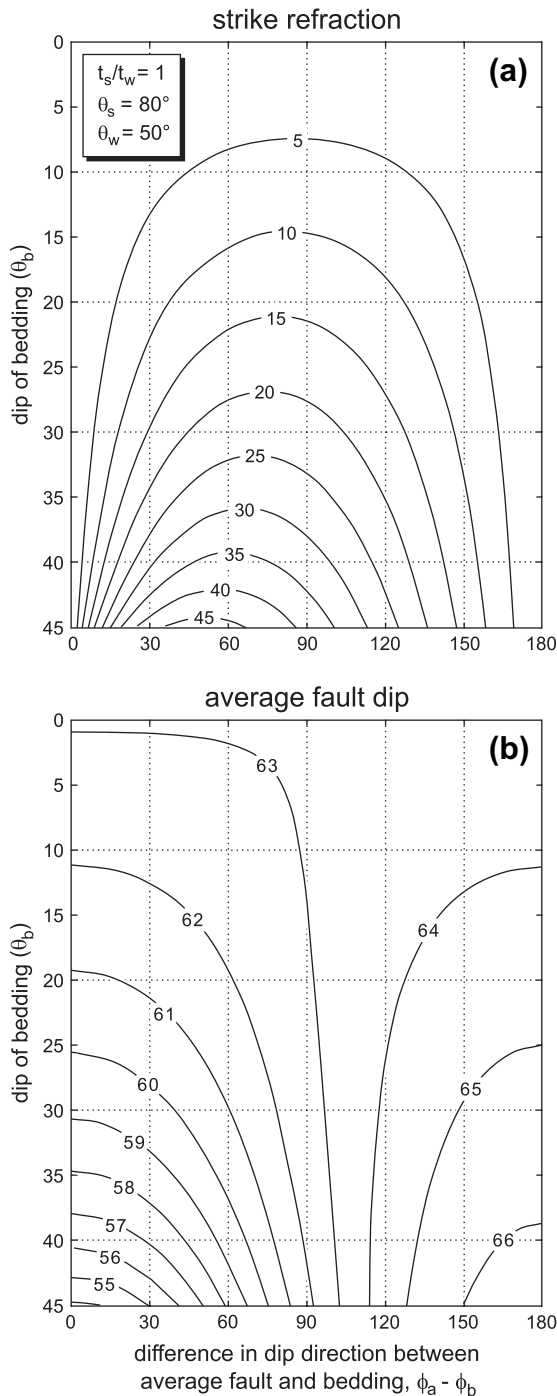$\theta_w = 50°$

average fault dip

(b)

Fig. 5. Plot of dip of bedding versus difference in dip direction between average fault and bedding contoured for (a) strike refraction, $\phi_s - \phi_w$ and (b) average fault dip, θ_a. Fault dips are 80° and 50° in the strong and weak layers, respectively, and the thickness ratio, t_s/t_w, is 1.0. All contour labels are in degrees.

opposite direction to the average fault. Maps constructed using the strike-change data obtained from this approach are shown in Fig. 6a. These maps illustrate the zigzag geometry of the fault trace (strike refraction) and also show that the amount of strike refraction increases with increasing dip of bedding (Fig. 5a). The cross sections (Fig. 6b) show that the average

difference in dip direction between average fault and bedding, $\phi_a - \phi_b$
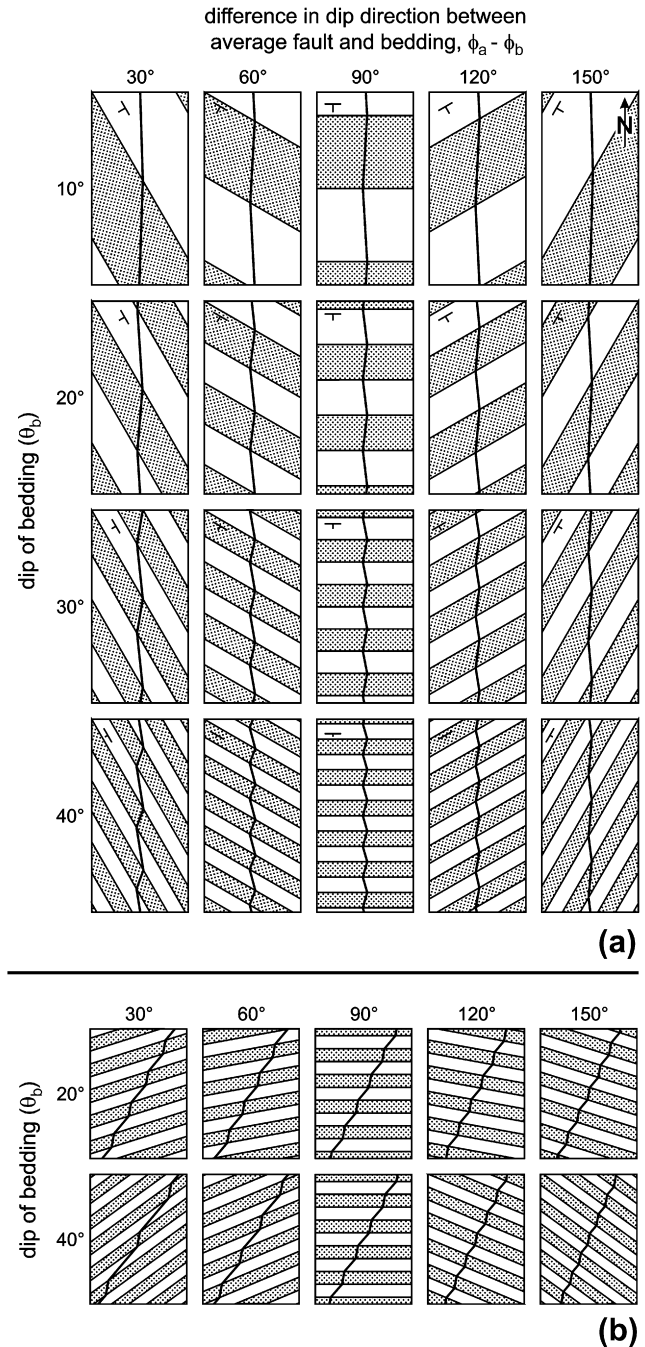

(a)

(b)

Fig. 6. (a) Maps and (b) cross sections of continuous refracting faults for various orientations of bedding. Fault dips in the strong (stippled) and weak layers (unornamented) are 80° and 50°, respectively, and the thickness ratio is 1.0. The average fault dips towards the west in all maps and the strike and dip symbol gives the orientation of bedding. The maps were drawn using the numerical results shown in Fig. 5.

amount of refraction increases with increasing dip of bedding (Fig. 5a). Fig. 5b shows that the average fault dip is a function of bedding orientation, though for the particular geometrical parameters chosen it only varies by about 10°. Additionally Fig. 5b reveals that for a particular dip of bedding the average fault dip attains its maximum value when bedding dips in the

fault dip increases as the difference in dip direction between the average fault and bedding increases (Fig. 5b).

As stated above, we selected a thickness ratio of 1.0 and fault dips in the strong and weak layers of 80° and 50°, respectively, to illustrate the range of continuous fault geometries that are obtained when the orientation of the bedding is varied. The dependencies obtained (Figs. 5 and 6) also hold for different values of θ_s, θ_w and t_s/t_w, though the geometrical details will vary as a function of these three parameters. We therefore investigated the impact of thickness ratio and dip refraction on fault geometry. Fig. 7a shows three map view examples of continuous refracting faults in periodically layered sequences with thickness ratios of 0.1, 1.0 and 10. The graphs in Fig. 7b and c show the differences in dip direction between the fault contained in the strong and weak layers and the average fault as a function of thickness ratio. In Fig. 7b the fault dips in the strong and weak layers are 80° and 50°, respectively, and the dip of the bedding is 30° for five different orientation of bedding (i.e. for the maps shown in the third row in Fig. 6a). Curves are plotted for five different orientations of bedding. We also investigated the effect of fault dips in the strong and weak layers (fault dip refraction) and thickness ratio on strike refraction (Fig. 7c) for a dip of bedding of 30° and strike difference between average fault and bedding of 90°; i.e. we vary both the thickness ratio and the fault dip refraction for the central map in the third row in Fig. 6a. The strike refraction in these graphs is the distance between corresponding labelled curves and varies slightly as a function of thickness ratio. The change in fault strike in the different lithologies ($\phi_s - \phi_a$ and $\phi_w - \phi_a$), however, strongly depends on the thickness ratio (Fig. 7). The maps and curves reveal that fault strike changes are typically greater in the less abundant material (see Fig. 7a). Additionally Fig. 7c reveals that the greater the dip refraction the greater the associated strike refraction.

Although this section highlights some interesting geometrical properties of continuous refracting faults, it is not yet clear whether these types of geometries often occur in nature. As a consequence, we have extended the results obtained in this section to consider a more likely geometrical model in which segmented arrays of faults, rather than continuous refracting faults, arise from the associated complications of differing fault and bed orientations (Fig. 3c).

4. Discontinuous refracting faults

4.1. Geometry

The zigzag fault geometry predicted by the continuous fault model (Fig. 6a) implies that the fault has oblique-slip components, which are in opposite senses in the strong and weak layers. Field evidence and numerical modelling of small-scale normal faults in high strength contrast multilayer sequences suggest that normal faults first localise within the strong/brittle layers as steeply dipping dip-slip faults or extension fractures, which are later linked via shallow dipping faults in the weak/ductile layers (Peacock and Zhang, 1993; Crider and Peacock,
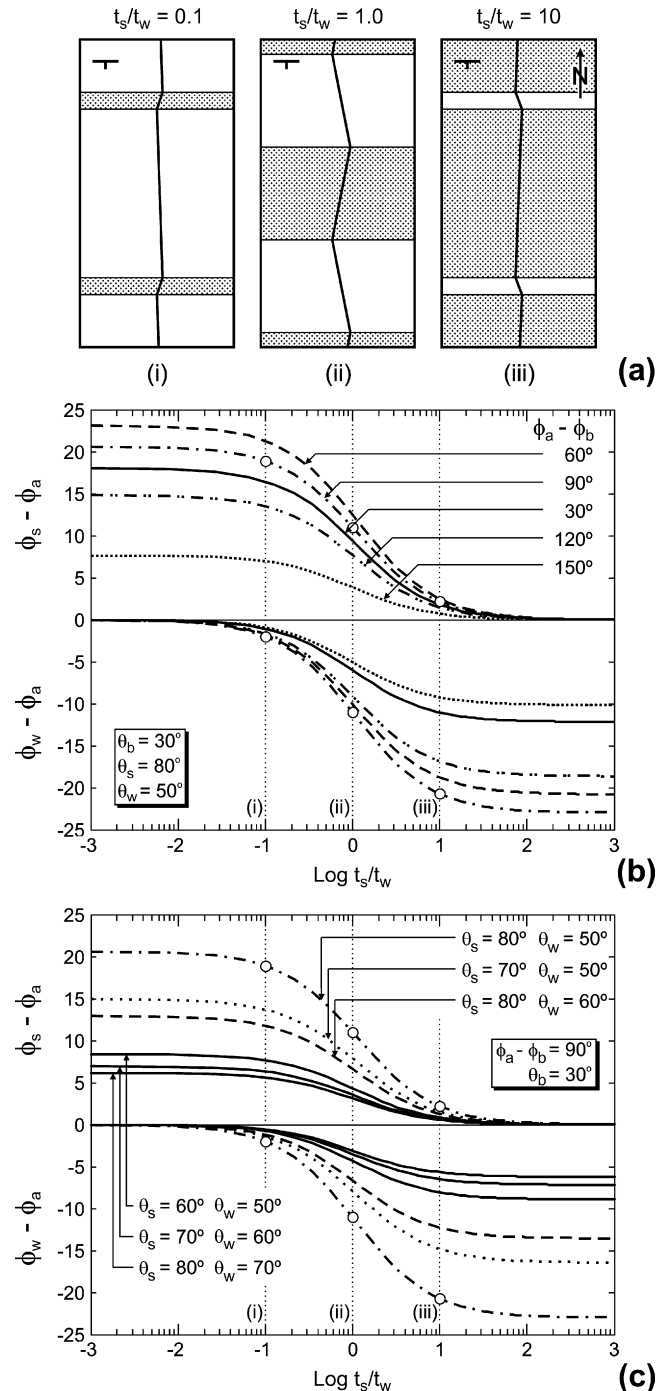

Fig. 7. Maps and graphs illustrating the impact of thickness ratio on the geometry of continuous refracting faults in periodically layered sequences. (a) Three map view examples for thickness ratios of 0.1, 1.0 and 10. Fault dips in the strong (stippled) and weak layers (unornamented) are 80° and 50°, respectively, the average fault dips towards the west and bedding dips 30°S. (b and c) Plots of differences in dip direction between the average fault and faults contained within the strong and weak layers, $\phi_s - \phi_a$ and $\phi_w - \phi_a$, versus log thickness ratio, t_s/t_w, calculated for (a) five different $\phi_a - \phi_b$ values and (b) selected dips within the strong and weak layers. In (b) the fault dips in the strong and weak layers are 80° and 50°, respectively, and the dip of bedding is 30°. In (c) the difference in dip direction between the average fault and bedding is 90° and the dip of bedding is 30°. The strike refraction for a given t_s/t_w ratio is the angular difference between corresponding labelled curves for the strong and weak layers. The intersections of the curves with the labelled vertical dashed lines (white dots) are the data used for constructing the maps shown in (a).

2004; Schöpfer et al., 2006). Therefore a more realistic and our favoured initial geometry is that the fault localises in the strong layers as dip-slip faults with dip directions parallel to the average fault, which, in dipping layers, is only possible if it forms an en échelon array. In these circumstances, the 3D geometry of segmented refracting faults are related to and can be derived from those of the continuous faults shown in Fig. 3b and described in the previous section. Assuming that the fault in the strong layers localises as an en échelon array of dip-slip faults and that these segments have the same dip direction as the average fault, then the median plane through the en échelon array will have the same orientation as the continuous fault (within the strong layers) in Fig. 3b. We use the term median plane in this work to refer to the plane containing the displacement vectors at the centres of each segment within individual layers. Unlike the 'average' plane, used to describe the overall orientation of a refracting fault, the 'median' plane is therefore specific to the individual layers and will differ between the strong and weak layers. In the following it is only discussed with reference to the strong layers. A block diagram showing a fault array geometry that satisfies these requirements is shown in Fig. 3c. In the following sections we use our simple geometric model to quantify the degree of segmentation in map view as a function of bedding orientation. A prerequisite of this exercise is, however, to define geometrical parameters that describe the geometry of en échelon arrays.

4.2. Overlap length and fault separation

The geometry of fault arrays with en échelon geometry can be described using the following parameters, all of which are measured in a horizontal plane in this study: (i) fault segment length, L, (ii) overlap length, O, which is the length of the rectangular region that is bounded by two neighbouring segments, (iii) separation, S, which is the normal distance between two neighbouring segments, and (iv) the difference in strike between the individual fault segments and the average fault array, ψ (Fig. 8a). These four parameters are related by the simple relationship

$$S = (L - O)\tan\psi. \tag{2}$$

Although the geometry of an en échelon array can therefore be fully described by three parameters, the number of parameters can be reduced to two by introducing the overlap length to separation ratio, O/S, which is often 2−4 for natural and experimental normal fault arrays (Soliva and Benedicto, 2004; Hus et al., 2005). The en échelon arrays shown in Fig. 8 were drawn using Eq. (2) for constant segment lengths L (Fig. 8b) and for constant separations S (Fig. 8c), for different values of ψ and O/S. From these maps one can conclude that as the inclination of the segments, ψ, increases the degree of segmentation increases, regardless of whether we keep the segment length or the separation constant.
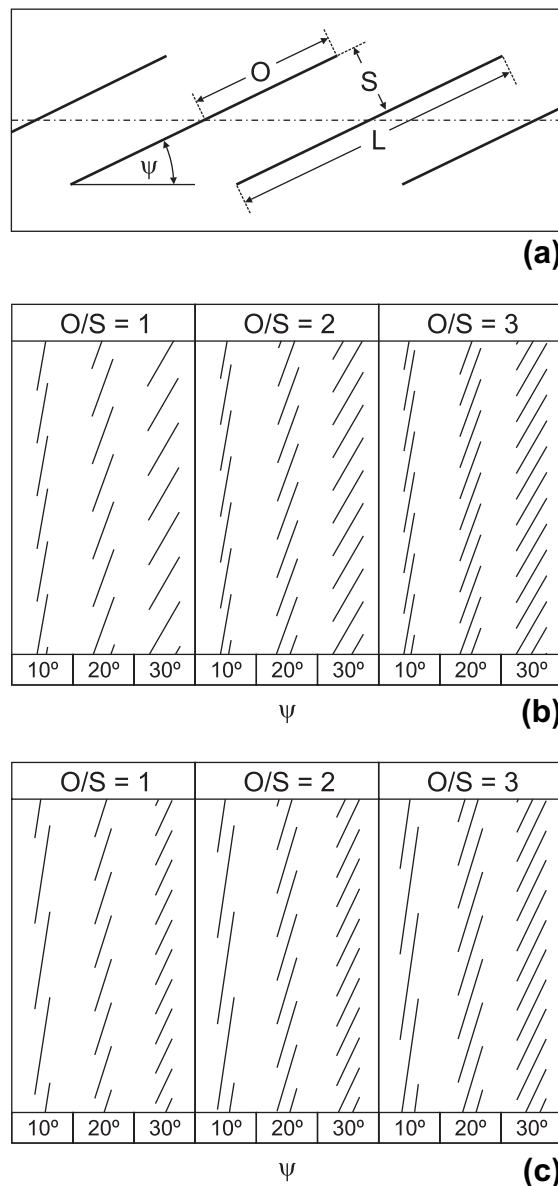

Fig. 8. (a) Diagram illustrating the nomenclature used to describe en échelon arrays. (b) Illustration of the variation in fault array geometries for constant segment length, L, three different ψ-values and three different overlap to separation ratios. (c) Illustration of the variation in fault array geometries similar to those shown in (b) for constant separation, S.

4.3. Maps of discontinuous faults

As stated above we assume that the fault segments within the strong layers have the same dip direction as the average fault since they nucleate as dip-slip faults. The strike differences between the average fault and the faults in the strong and weak layers, $\phi_s - \phi_a$ and $\phi_w - \phi_a$, respectively, that were obtained for continuous faults can then be used to construct maps of discontinuous faults using Eq. (2) (see Fig. 8). This requires that we keep the overlap to separation ratio and the length of one parameter in Eq. (2) constant. For direct comparison with the continuous fault results, we have chosen a thickness ratio of 1.0. Median planes through the en échelon arrays within the strong layers have a dip of

80° and the faults within the weak layers have a dip of 50°. Fig. 9a shows maps constructed for strong layers using the data obtained from the analysis of continuous faults and using Eq. (2) with a constant separation and an overlap to separation ratio of three (Fig. 8c); note that these maps are not horizontal slices (as shown in Fig. 6a), but are top views of the bedding plane. Essentially, these maps are aerial views of the top of a strong layer within a multilayer, where the overlying layers have been eroded. Consequently, cut-effects arise in these maps, e.g. the segment traces are not oriented N-S, despite the fact that their dip direction is 270°. A line joining the centres of the fault segments in these maps is the intersection lineation of bedding with (i) the median plane through the en échelon segments, (ii) the faults in the weak layers and (iii) the average faults plane (Fig. 3c).

The maps show that degree of segmentation generally increases with increasing dip of bedding (Fig. 9a). The overall trends observed for the discontinuous faults (i.e. increasing segmentation with increasing dip of bedding and increasing discordance in dip direction between bedding and the average fault) are similar to the trends discussed above for continuous faults in which the discordance is accommodated by strike re-fraction. This similarity is inevitable since the strike-changes calculated for the continuous fault are used to determine (for a given O/S ratio) the degree of segmentation in the discontinuous case. Hence the sensitivity study of geometrical parameters presented above for a continuous fault (Fig. 7) can be used to predict the degree of segmentation. Therefore, for example, we can infer that refracting faults within dipping multilayers are expected to exhibit a higher degree of segmentation in the less abundant lithologies. Cross sections of segmented faults shown in Fig. 9b were constructed by randomly selecting sections along the maps shown in Fig. 9a and by using the same bedding geometries as shown for continuous faults in Fig. 6b. We did not introduce another parameter that takes into account the separation of the segments as a function of bed thickness since for these circumstances no clear relationship may exist between fracture spacing and bed thickness. Despite these limitations, the cross sections shown in Fig. 9b illustrate that the frequency of occurrence of two segments within a strong layer generally increases with increasing bed dip.

In this section we only investigated the degree of fault segmentation within the strong layers. Maps and cross sections similar to Fig. 9 can also be determined for the weak layers. The general results obtained for the strong layers also hold for the weak layers, though the stepping direction of the fault segments will be in the opposite direction. This is because the median planes through the en échelon arrays in our discontinuous model are the solutions for the continuous fault model, where the faults in the two different lithologies exhibit strike changes in opposite direction (Figs. 3b and 4d). Although our method allows us to determine a segmented geometry for the weak layers, we expect that in nature the geometry of faults within the weak layers will be largely controlled by the requirement to link earlier formed segments in the strong layers.
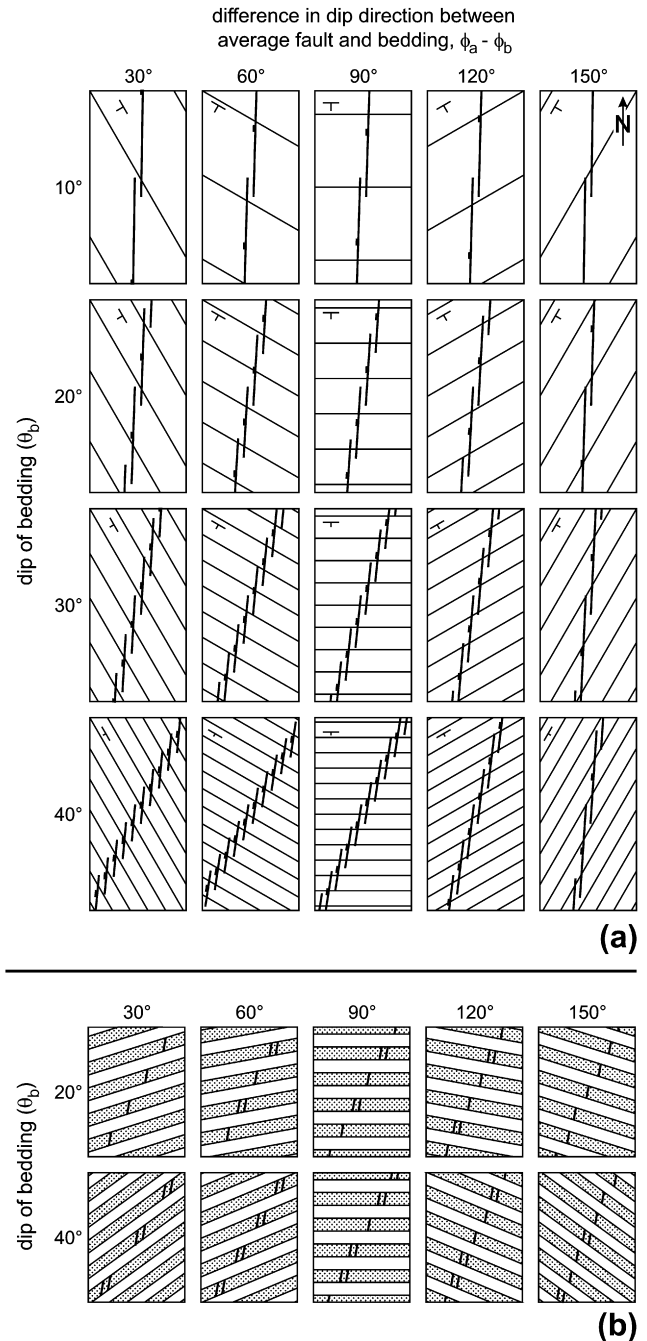

(a)

(b)

Fig. 9. (a) Maps of en échelon fault arrays exposed at the top of the strong layers as a function of bedding orientation relative to the average fault. The average fault strikes N-S and dips towards the west. Thickness ratio, t_s/t_w, is 1.0. The overlap length to separation ratio is 3.0 and the size of the relays (i.e. rectangular overlap region) is held constant. Bold lines are traces of fault segments (tick towards hangingwall) and thin lines are structure contours of the bedding plane. The dip of median planes through the layer-bound fault ar-rays is 80°. Similar maps can be constructed for the weak layers. Note, how-ever, that en échelon faults exposed on top of the weak layers would exhibit the opposite stepping. (b) Cross sections of the fault geometries shown in (a). Cross sections are drawn normal to the strike of the average fault and for each layer a section was randomly selected from the maps shown in (a). Since faults within a mechanical multilayer typically localise first within the strong layers as (Mode I) fractures, only faults within the strong layers are shown.

5. Experimental modelling of discontinuous faults

5.1. Methodology and boundary conditions

The previous two sections considered continuous and discontinuous refracting faults, respectively, which could be considered either as geometrical end-members or as stages within a growth sequence. Many studies of natural faults have shown that faults often grow as initially segmented (discontinuous) arrays that are progressively linked with increasing displacement to form a continuous fault (e.g. Peacock and Sanderson, 1994; Childs et al., 1995, 1996). Although our geometrical analysis cannot predict whether faults in dipping multilayers are likely to be initially segmented or continuous, our preconception, based on outcrop studies of small scale faults, is that segmented faults are more likely. In this section, we therefore present a suite of small scale physical experiments with appropriate boundary conditions designed to test our simple geometrical model for the formation of segmented faults.

We used the sandbox modelling technique, a well-established method for modelling the development of faults in isotropic, homogeneous brittle rock (e.g. Mandl, 1988). The analogue material was dry quartz sand with a friction angle, φ, of $33 \pm 4°$. Normal faults that develop in this analogue material are expected to have a dip of $45° + \varphi/2$, i.e. approximately $61.5 \pm 2°$, according to the Coulomb–Mohr theory of faulting, and this value is confirmed in the models. A detailed account of the scaling of physical experiments and of the justification and limitations of using dry sand as an analogue material for brittle rock can be found in Mandl (2000, chapter 9).

In this study we investigated the propagation of predefined 'basement' faults into a 'cover' sequence. There are a variety of scenarios for which our boundary conditions are appropriate, such as the reactivation of a faulted substrate overlain by an unfaulted sedimentary sequence. Alternatively the model could represent the propagation of a fault across the interface between two layers characterised by different mechanical properties and related fault dips. For simplicity we will refer to the rigid blocks containing the predefined faults as *base* and the overlying sand as *cover*; the boundary between these two 'units' is the *base–cover interface*.

In all of the three experimental configurations used, a central wedge-shaped base block (the hangingwall block) fits exactly between two footwall blocks (Fig. 10). The two predefined faults have a dip of $45°$ in all models and the dips of the base–cover interface are 0, 10 and $20°$ (Fig. 10a, b and c, respectively). The dip directions of the predefined faults and the base–cover interfaces are perpendicular to each other, so the intersections of the inclined base–cover interfaces (Fig. 10b and c) with the predefined faults are therefore not horizontal, a feature which will be discussed below. The base blocks are confined laterally by glass plates and whilst one of the footwall blocks is fixed, the other is connected to a geared motor. The cover sequence consists of alternating layers of coloured loose sand, each layer of which is prepared by scraping piles of loose sand to the desired
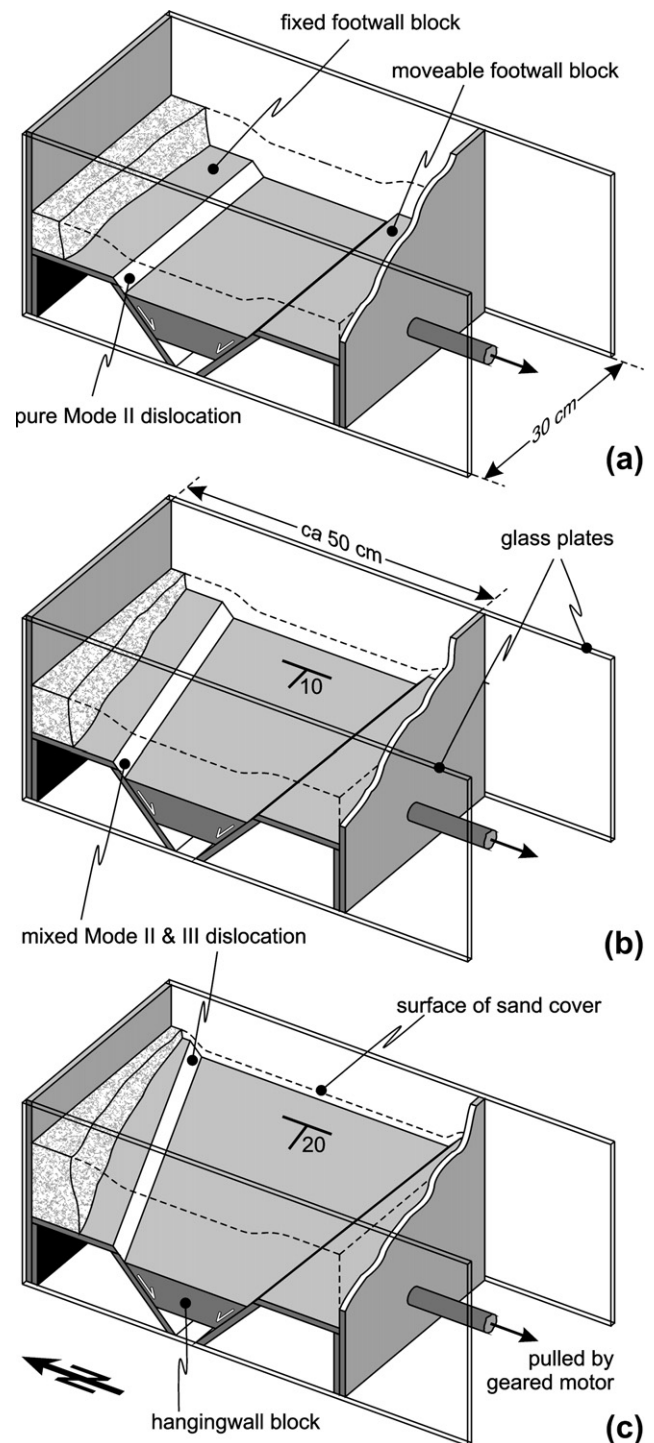

Fig. 10. Diagrams illustrating the experimental set-ups for the three different sandbox models designed to test our geometrical approach. The models are shown at a finite throw of 2 cm and the sand cover is only partly shown (the surface of the deformed sand cover is schematically shown as dashed line). The dips of the base–cover interface are 0, 10 and 20° in (a), (b) and (c), respectively. The sand cover in (a) had a uniform thickness of 6.1 cm. The sand covers in (b) and (c) were wedge-shaped, 7.7 cm thick in the west and 2.5 cm thick in the east in (b), and 12.2 cm thick in the west and 1.3 cm thick in the east in (c). See text for further explanation.

thickness. Faulting within the cover sequence is achieved by pulling the moveable footwall block with a velocity of *ca* 10 cm/h; as a consequence the hangingwall block slides downwards under its own weight. At the start of each experiment the predefined faults have no throw.

Our model configurations enforce fault refraction at the base–cover interface, because the predefined faults have a 45° dip, which is lower than the dip of normal faults that develop within the cover sequence (expected fault dip of 62°). Furthermore, relative to the intersection between the predefined fault and the base–cover interface, the mode of faulting changes with the dip of the base–cover interface. For example, in the case of a horizontal base–cover interface the predefined fault represents a Mode II dislocation, since the slip vector is perpendicular to the fault–interface intersection (Fig. 10a). For a dipping base–cover interface, the predefined fault is a mixed Mode II and III dislocation, since the slip vector is oblique to the fault–interface intersection (Fig. 10b and c). Each model was extended by the same amount of bulk extension (40 mm), with each predefined fault having a final throw of 20 mm at the base–cover interface. The surface of each model was photographed in 2 mm throw intervals. Once completed, each model was saturated with water so that vertical sections could be generated and photographed for subsequent analysis. Since the resulting fault pattern in each model is symmetrical, we only present the results for one fault zone from each configuration.

5.2. Stereonet prediction

As a prelude to presenting our model results, stereonet solutions, based on our geometrical model, can be constructed for each experimental set-up (left column in Fig. 11). For convenience we choose a geographic reference frame where the predefined fault with the fixed footwall block dips towards the south (180/45; Fig. 10). In the case of an inclined base–cover interface, the interface dips towards the west (270/10 and 270/20, Fig. 10b and c, respectively). The plunge direction and plunge of the predefined fault/base–cover interface intersections for the three configurations are therefore (270/00), (260/10) and (250/19). In addition we can assume that antithetic faults, which nucleate at these intersections, will develop in the cover sequence due to the change in fault dip (i.e. at the kink of the sliding path as referred to by Mandl, 1988). A continuous refracting fault demands that the intersection of the cover faults be the same; consequently, using a dip of 62°, the dip directions of the syn- and antithetic faults can be constructed and are 180° (no strike change) in case of the horizontal base–cover interface, 175° (synthetic) and 345° (antithetic) for the 10° dipping interface, and 170° (synthetic) and 330° (antithetic) for the 20° dipping interface (Fig. 11). If our geometrical model is valid, we therefore expect the following: (i) neither strike change nor systematic stepping of faults developing in the cover above the horizontal interface (Fig. 11a), and (ii) either left-stepping dip-slip fault segments or continuous dextral-oblique-slip normal faults within the cover above the inclined interfaces (Fig. 11b and c).

5.3. Experimental results

5.3.1. Horizontal base–cover interface

The earliest faults which intersect the surface of the model are steep synthetic faults, referred to as precursor faults in the literature (e.g. Horsfield, 1977). With increasing displacement, one and sometimes two shallower dipping synthetic faults develop in the footwall. Precursor faults do not extend along the entire length of the predefined fault and subsequently link along strike with shallower dipping synthetic faults to form undulating fault traces in map view (Fig. 11a). Although this type of fault segmentation leads to the formation of short-lived relay zones, stepping of these fault segments is not systematic. With increasing displacement a single through-going and straight master fault develops in the footwall of the precursor faults and the fault scarp gradually collapses. The master fault has a dip of *ca* 60° as expected from the friction angle of the sand. Two or three antithetic adjustment faults also develop within the models. New antithetic faults develop in the hangingwall of earlier antithetics, and, together with contemporaneous slip along synthetic faults, lead to the formation of a secondary graben (see cross section in Fig. 11a).

5.3.2. Dipping base–cover interface

Models with a dipping base–cover interface have a wedge-shaped cover sequence, which thins towards the east (Fig. 10b and c). Although faults in the thinner parts of the cover show more advanced stages of fault growth, the fault pattern is similar for a given throw to cover thickness ratio. For a 20° dipping interface, initially E-W striking precursor faults exhibit a systematic segmented left-stepping geometry (at predefined fault throws of *ca* 4 mm; Fig. 12). With increasing displacement, the western tip of each segment typically propagates towards the west, whereas the eastern tip propagates towards the NE to link with another segment (at throws of *ca* 8 mm; Fig. 12). The linkage leads to hangingwall breaching of individual relay zones, with hangingwall segments propagating and linking with the footwall segments. Further displacement causes rotation of the breached relay zones, which only ceases when a through-going synthetic master fault is developed, and the array of precursory structures becomes inactive: because of fault scarp collapse, abandoned splays are not as easily seen where the fault scarp is first developed and where the cover is thinner. The average dip of this complex synthetic master fault zone is *ca* 60° and the dip direction is in perfect agreement with our stereonet prediction, i.e. 170° (Fig. 12). Two or three antithetic faults develop, which exhibit systematic stepping on the mm-scale, a feature which cannot therefore be seen from the photographs. The dip directions of the antithetic fault arrays are in agreement with our stereonet prediction, i.e. 330°. The model with a 10° dipping interface is, as predicted, characterised by a similar fault evolution but with a less dramatic change in dip direction relative to the predefined fault and with the development of fewer relays (Fig. 11b). In both models, contemporaneous movement along synthetic and antithetic faults leads to the formation of

Stereonet prediction

Map view at a throw of 6 mm

Cross section at a throw of 20 mm

Key for poles and great circles

● ──── synthetic cover fault ○ ·─ ─ ─ ─ antithetic cover fault ■ ·─·─·─· predefined fault
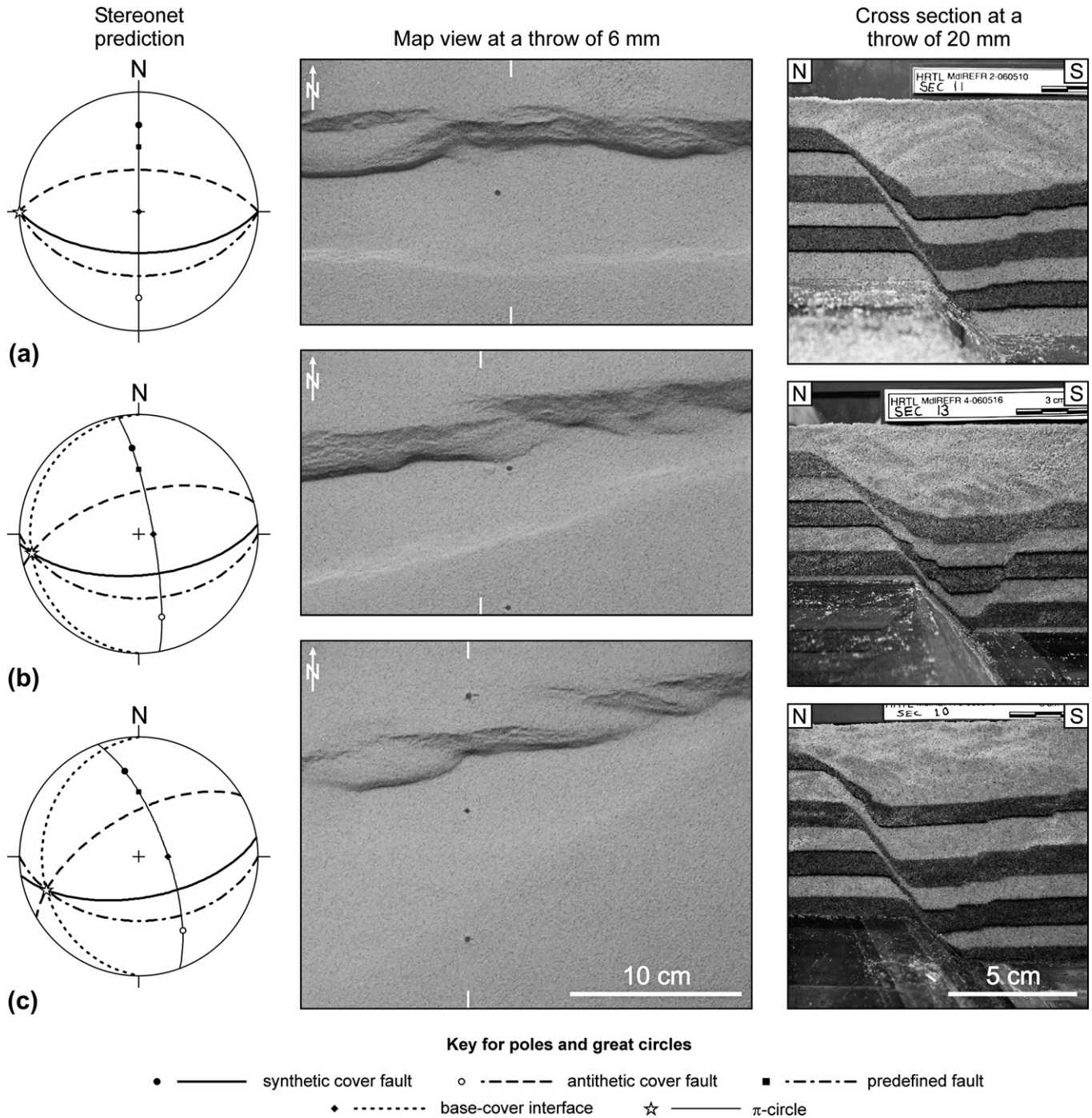
◆ ········ base-cover interface ☆ ──── π-circle

Fig. 11. Stereonet predictions of fault orientations in the sand cover (using a fault dip of 61.5°), map view of models at a throw on the predefined fault of 6 mm, and cross sections at a finite throw of 20 mm for the three different experiments (see Fig. 10 for boundary conditions). Only the centre of each model is shown in map view and ticks in the map views indicate locations of cross sections.

a secondary graben that narrows towards the east, i.e. towards the thinner part of the model.

6. Interpretation of natural example

In the previous sections we introduced a simple model for the formation of segmented normal faults arising from fault re-fraction. We later verified our model using a suite of physical experiments. In light of our model we now re-examine the field example (Fig. 1) of an oblique-sinistral normal fault within a limestone/shale multilayer sequence at Kilve fore-shore, Somerset, UK (see Glenn et al., 2005, for geological background of this area). The fault zone exhibits fault dip re-fraction (Fig. 1b) with an average fault dip difference between the limestone and shale beds in the range of 20–30°, and map view segmentation with right-stepping segments (Fig. 1c).
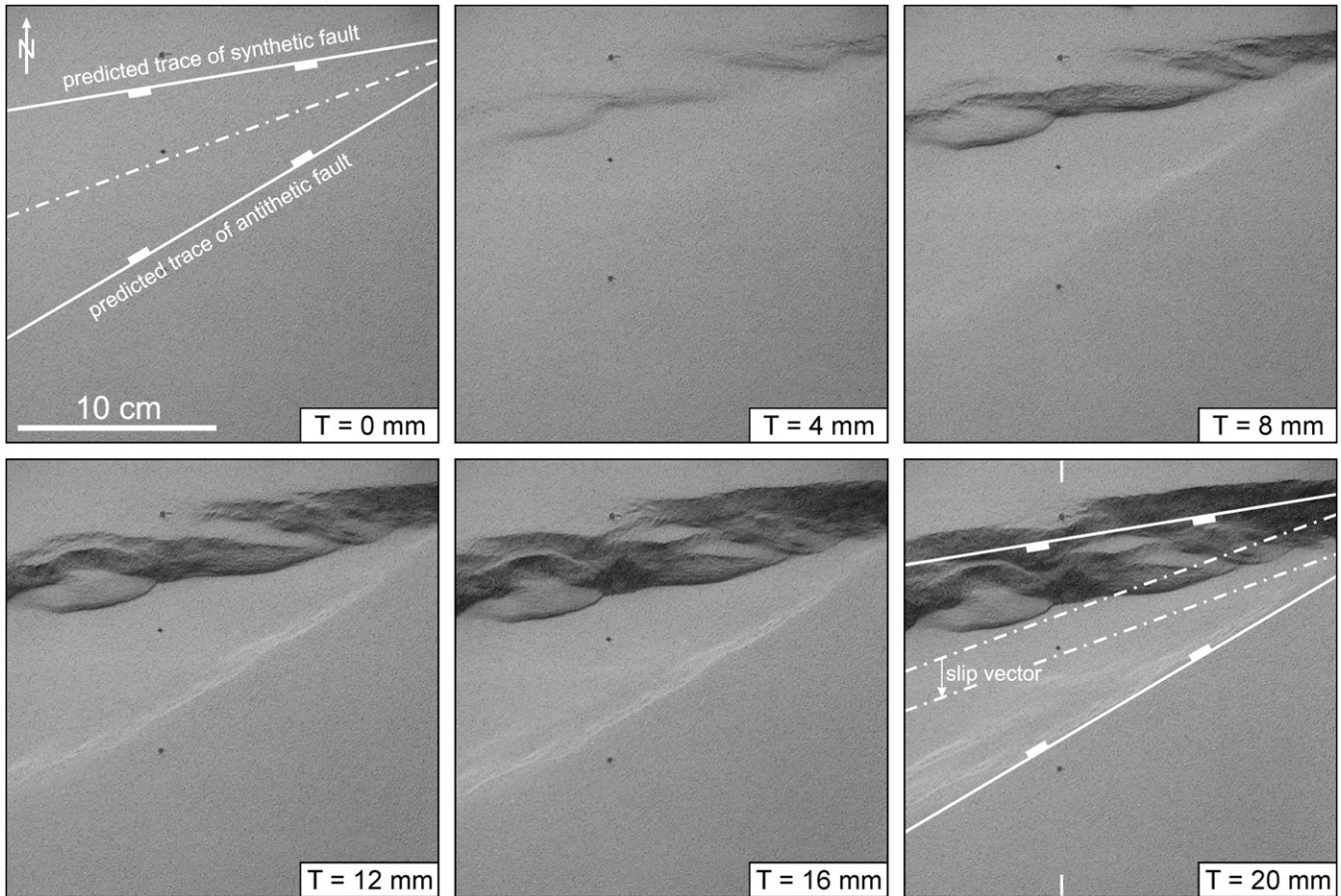
Fig. 12. Photographs of the top surface of sand cover above 20° dipping base–cover interface (see Figs. 10c and 11c). The throw (*T*) of the predefined fault at the different stages of model evolution is shown. The dash-dot line at a fault throw of 0 mm is the intersection between the predefined fault (dipping 45°S) and the base–cover interface (dipping 20°W); the solid lines are the predicted traces of the syn- and antithetic fault with ticks towards secondary graben. The predictions of fault orientations are also shown at a finite fault throw of 20 mm, together with the footwall and hangingwall cut-offs of the predefined fault (dash-dot lines). The secondary graben diverges towards the west, where the cover is thicker.

Within the shale layers, good kinematic indicators (slickensides) are exposed, whereas within the limestone layers calcite infilled pull-aparts are present that are attributed to pre-cursory extension fracturing (Fig. 1a). Orientation data for the fault zone are shown in Fig. 13a, together with the mean orientations of bedding, faults within the limestone and shale, and a slickenside lineation within the shale. The orientation data show that there is a strike difference between the faults in the limestone and shale layers and that the slip vector is oblique to fault/bedding intersections. Although this fault zone therefore represents a good field example for testing our model, ready comparison with our model and with associated stereonets (Fig. 4) is made much easier by rotation of the slickenside lineation, together with associated orientation data, so that (i) the fault in the shale is dip-slip with a dip of 50° and (ii) bedding is dipping towards the south (Fig. 13b). Using the intersection lineation between bedding and the fault within the shale, we constructed a continuous refracting fault with a fault dip within the limestone layers of 80°. The strike difference between the fault within the shale and the constructed continuous fault within the limestone layers is 24° (Fig. 13b). According to our model, therefore, we would

expect a high degree of fault segmentation, with right-stepping segments within the limestone layers, and this is exactly what we observe (Fig. 1c). The measured mean dip direction of the fault segments within the limestone ($\phi = 271$) is slightly different to the dip direction predicted for a continuous fault ($\phi = 282$; Fig. 13b). This reflects the fact that the fault is segmented and exhibits systematic stepping, with segments that strike almost sub-perpendicular to the extension direction.

7. Discussion

Fault refraction is a well-documented feature of normal faults contained in multilayer sequences and occurs on a large range of scales (mm–km). Best seen on cross-sectional views of faults, refraction is most often a response to different mechanical properties of different lithologies (fault refraction due to differential compaction after faulting, e.g. Davison, 1987, is not discussed here). By contrast, another propagation-related phenomenon, fault segmentation, is best seen in map view of normal faults and is also a common feature of normal faults, at least in their earliest stages of growth. In this paper we have developed a simple geometric model of
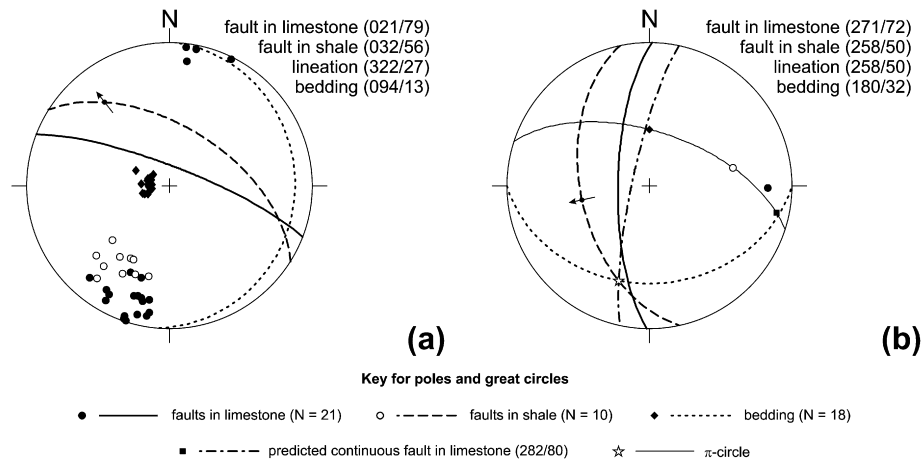
Fig. 13. Lower hemisphere, equal area stereographic projections of orientation data of mapped fault zone shown in Fig. 1. In (a) the raw data are shown, together with great circles of the mean orientations, and a slickenside lineation within the shale. In (b) the average orientations and the lineation are rotated so that the fault within the shale is dipping 50° and is pure dip-slip and bedding is dipping towards the south (these rotations permit easy comparison with the model geometries of Figs. 3 and 4). Note that our geometrical model would predict fault segmentation, with right-stepping segments (see relay ramp in Fig. 1c).

normal faults which suggests that fault segmentation and/or strike refraction are inevitable consequences of fault dip refraction within dipping multilayer sequences. This geometrical model provides a means of estimating the geometry of 3D fault refraction, and/or segmentation, within multilayered sequences, an approach we have tested using a series of plane strain physical experiments of faulting within a cover sequence above an underlying predefined fault. Our simple model suggests that the degree of fault segmentation and/or strike refraction will increase with increasing dip refraction between layers, a feature that will be promoted by high strength contrasts between layers. A continuous refracting (non-segmented) fault in a multilayer may be the exception rather than the rule, and lithological/mechanical stratigraphy is an extremely important factor for understanding the segmented nature of faults.

The physical experiments support our geometrical approach and demonstrate, for example, that systematic stepping of fault segments in the cover above a shallow dipping predefined fault is not necessarily a kinematic indicator for oblique-slip reactivation. In circumstances where the orientation of the predefined faults and the cover–base interface are poorly constrained, we advise caution regarding the interpretation of fault kinematics from systematic stepping fault segments.

Mandl (1987) has shown that faults contained in an isotropic, homogeneous material will be discontinuous if continuous principal planes of stress cannot be defined (see also Treagus and Lisle, 1997). This result obviously raises the following question: What controls fault segmentation, non-plane stress fields or lithological/mechanical contrasts? The answer is probably both. Non-plane stress fields arise during lateral propagation of normal faults (screw dislocation; Cox and Scholz, 1988). However, they also develop if all principal axes of stress are oblique to interfaces of materials with contrasting mechanical properties (Treagus, 1981, 1988). In both cases, continuous principal surfaces of stress cannot be defined, which will most likely result in the formation of

discontinuous faults. It is not yet established whether the propagation process or mechanical stratigraphy is the dominant cause of fault segmentation.

The synthetic fault arrays developed in the experimental models with inclined base–cover interfaces are initially highly segmented with adjacent segments separated by relay zones which are progressively breached to form a through-going fault. Although these fault growth stages are widely recognised, there is still an ongoing debate whether segmented normal fault arrays are the result of linkage of initially isolated faults or whether the segments were always part of the same fault zone, i.e. the faults are kinematically coherent (Walsh et al., 2003). Since in our models the individual segments are part of the same fault zone, the modelling results clearly favour the latter.

Our simple model provides geometrical predictions that are consistent with a natural fault zone within a limestone/shale sequence (Figs. 1 and 13). Stepping directions and, in particular, the degree of fault segmentation of normal faults are, however, likely to be also controlled by factors other than differences in the dip direction of fault and bedding. Although further research is required into the origin and nature of 3D changes in principal stress directions and discontinuous principal stress planes across interfaces within heterogeneous rock volumes, our experimental models, for which the boundary conditions were fully controlled, provide strong support for the importance of fault/bed geometrical configurations in the generation of segmented faults within multilayered sequences.

8. Conclusions

- A simple geometric model suggests that continuous normal faults exhibiting fault dip refraction in multilayers will also exhibit strike refraction if bedding is dipping and has a different strike to the fault zone. The amount of strike refraction is mainly a function of fault dip refraction and the orientation of bedding relative to the fault.

- The geometric model can be used to estimate the degree of fault segmentation, if it is assumed that faults nucleate first as dip-slip or extensional structures within the mechanically stronger lithology. Normal faults are expected to be segmented if bedding is dipping and has a different strike to the fault zone. The degree of segmentation is a function of bedding orientation, fault dip refraction and thickness ratio of the strong and weak layers comprising the multilayer.
- Our model of fault dip refraction and fault segmentation and/or strike refraction has been verified using a simple physical experiment, which shows that fault refraction in dipping layers causes fault segmentation with predictable directions and degrees of stepping.
- Both experimental and geometrical evidence suggest that systematic stepping of normal faults in cover sequences above a predefined fault, such as a reactivated basement fault, is not necessarily an indicator of oblique-slip reactivation.
- Direct application of the model to natural fault zones is likely to be complicated by the operation of other factors that also control fault segmentation and/or strike refraction.

Acknowledgements

Appendix A. Derivation of Eq. (1)

The aim of this appendix is to derive an equation that can be used to construct the geometry of a continuous refracting fault in a periodically layered sequence. A list of symbols is provided in Table 1, and Fig. A1 shows both map view and cross section of a continuous refracting fault within a periodically layered sequence, together with the stereonet solution (see Section 3.2). In order to construct this geometry we predefine the true dips of the fault within the two lithologies, θ_s and θ_w, and dip direction/dip of both bedding and average fault, ϕ_b/θ_b and ϕ_a/θ_a, respectively. The intersection of bedding with the average fault plane can then be used to determine the dip directions of the fault within the two lithologies, an exercise that can be easily done using a stereonet (see inset in Fig. A1 and Figs. 2–4). The thickness ratio of the two lithologies, t_s/t_w, cannot be obtained from the stereonet alone. However, an equation relating
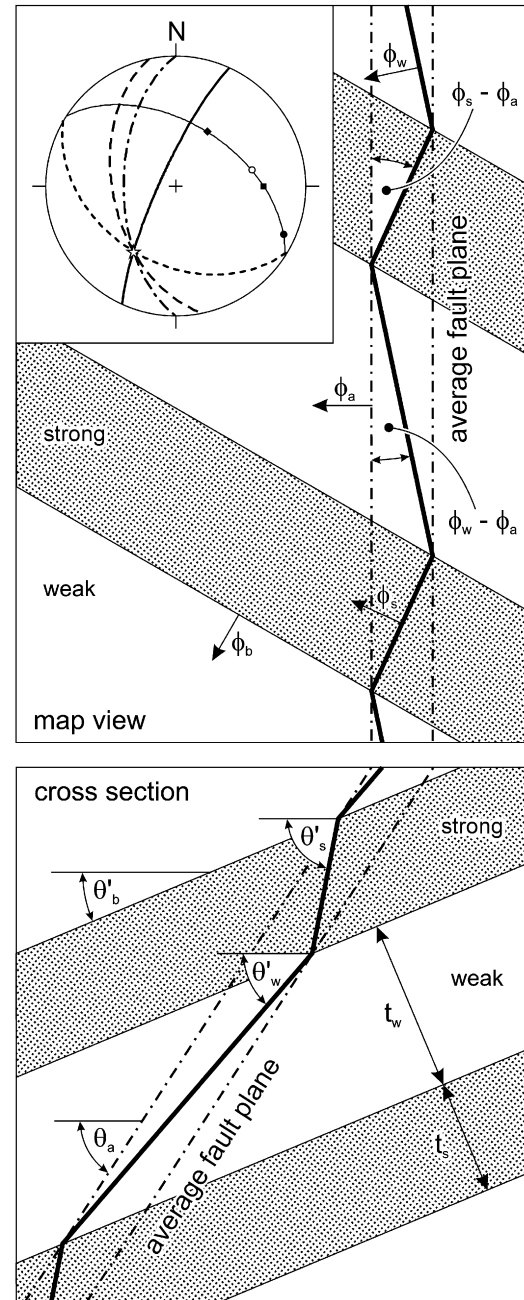

Fig. A1. Geometry of a continuous refracting fault in a periodically layered sequence as seen in map view and cross section. The true dips of the fault in the strong (stippled) and weak (unornamented) layers are 80° and 50°, respectively. Thickness ratio, t_s/t_w, is 2/3 and the difference in dip direction between the average fault (270/57) and bedding (210/40) is 60°. Styles of poles and great circles in stereonet are the same as in Figs. 2 and 4. Parameters used throughout the paper are labelled.

the orientations of fault and bedding to the thickness ratio can be easily derived in a cross section parallel to the dip direction of the average fault (Fig. A1). If the strike of dipping bedding is not parallel to the average fault, an apparent dip of bedding, (θ'_b) will be observed on the fault-normal cross section. As shown in this paper, this orientation of bedding relative to the average fault will cause a change in strike of the fault within the strong and weak layers (strike refraction) so that apparent
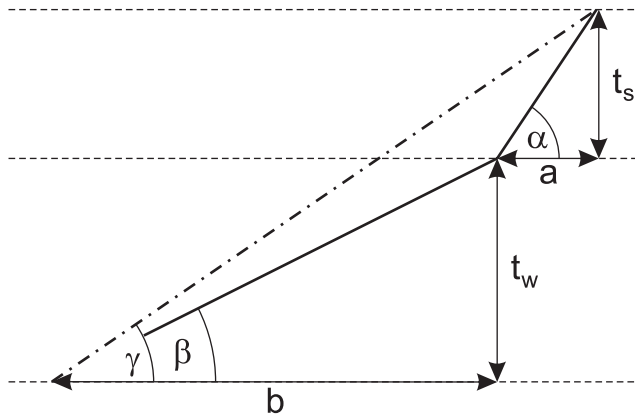
Fig. A2. Diagram showing a selection of angular relationships and parameters used in the derivation of Eq. (1). See Appendix A for further explanation.

dips, θ'_s and θ'_w, are observed in cross section (Fig. A1). The apparent dip, θ', of a plane in cross section can be obtained from the well-known relationship

$$\tan \theta' = \cos \delta \tan \theta, \tag{A1}$$

where θ is the true dip and δ is the difference between the dip direction of the plane and the strike of the cross section. The three apparent dips observed in cross section are therefore given by:

$$\tan \theta'_b = \cos(\phi_a - \phi_b)\tan \theta_b$$

$$\tan \theta'_s = \cos(\phi_a - \phi_s)\tan \theta_s$$

$$\tan \theta'_w = \cos(\phi_a - \phi_w)\tan \theta_w \tag{A2}$$

Also note that the layer thicknesses observed in cross section are apparent thicknesses if the bedding dip direction is not parallel to the strike of the cross section. The thicknesses observed in cross section are increased by a factor, which depends on the orientation of bedding relative to the cross section. Our aim, however, is to find an expression that relates the orientations of fault and bedding to the thickness ratio. Consequently, a factor correcting for apparent thickness will cancel out.

The derivation of the desired equation is simplified by subtracting the apparent dip of bedding, θ'_b, from the fault dips (Fig. A2):

$$\alpha = \theta'_s - \theta'_b \tag{A3a}$$

$$\beta = \theta'_w - \theta'_b \tag{A3b}$$

$$\gamma = \theta_a - \theta'_b \tag{A3c}$$

With the aid of the diagram shown in Fig. A2 three equations can be obtained:

$$\tan \alpha = t_s/a \tag{A4a}$$

$$\tan \beta = t_w/b \tag{A4b}$$

$$\tan \gamma = (t_s + t_w)/(a + b) \tag{A4c}$$

Substitution of Eqs. (A4a) and (A4b) into (A4c) and rearranging gives:

$$t_s \left(1 - \frac{\tan \gamma}{\tan \alpha}\right) = t_w \left(\frac{\tan \gamma}{\tan \beta} - 1\right) \tag{A5}$$

Finally, substitution of Eq. (A3) into Eq. (A5) and rearrangement gives the thickness ratio, t_s/t_w, as a function of fault and bedding orientation (Eq. (1)).

The dip directions of the fault in the strong and weak layers for a predefined thickness ratio can be obtained by systemically varying the average fault dip until the desired thickness ratio is obtained.

References

Childs, C., Watterson, J., Walsh, J.J., 1995. Fault overlap zones within developing normal fault systems. Journal of the Geological Society, London 152, 535–549.

Childs, C., Nicol, A., Walsh, J.J., Watterson, J., 1996. Growth of vertically segmented normal faults. Journal of Structural Geology 18, 1389–1397.

Cox, S.J.D., Scholz, C.H., 1988. On the formation and growth of faults: an experimental study. Journal of Structural Geology 10, 413–430.

Crider, J.G., Peacock, D.C.P., 2004. Initiation of brittle faults in the upper crust: a review of field observations. Journal of Structural Geology 26, 691–707.

Davison, I., 1987. Normal fault geometry related to sediment compaction and burial. Journal of Structural Geology 9, 393–401.

Dunham, K.C., 1948. Tyne to Stainmore. In: Geology of the Northern Pennine Orefield, vol. 1. Memoirs of the Geological Survey of Britain, London.

Dunham, K.C., 1988. Pennine mineralization in depth. Proceedings of the Yorkshire Geological Society 47, 1–12.

Ferrill, D.A., Morris, A.P., 2003. Dilational normal faults. Journal of Structural Geology 25, 183–196.

Glen, R.A., Hancock, P.L., Whittaker, A., 2005. Basin inversion by distributed deformation: the southern margin of the Bristol Channel Basin, England. Journal of Structural Geology 27, 2113–2134.

Goguel, J., 1982. Une interprétation méchanique de la réfraction de la schistosité. Tectonophysics 82, 125–143.

Horsfield, W.T., 1977. An experimental approach to basement-controlled faulting. Geologie en Mijnbouw 56, 363–370.

Hus, R., Acocella, V., Funiciello, R., De Batist, M., 2005. Sandbox models of relay ramp structure and evolution. Journal of Structural Geology 27, 459–473.

Imber, J., Tuckwell, G.W., Childs, C., Walsh, J.J., Manzocchi, T., Heath, A.E., Bonson, C.G., Strand, J., 2004. Three-dimensional distinct element modelling of relay growth and breaching along normal faults. Journal of Structural Geology 26, 1897–1911.

Jackson, P., 1987. The corrugation and bifurcation of fault surfaces by crossslip. Journal of Structural Geology 9, 247–250.

Larsen, P.-H., 1988. Relay structures in Lower Permian basement-involved extension system, East Greenland. Journal of Structural Geology 10, 3–8.

Mandl, G., 1987. Discontinous fault zones. Journal of Structural Geology 9, 105–110.

Mandl, G., 1988. Mechanics of Tectonic Faulting. Models and Basic Concepts. Elsevier, Amsterdam.

Mandl, G., 2000. Faulting in Brittle Rocks. Springer, Berlin/Heidelberg/New York.

Peacock, D.C.P., Sanderson, D.J., 1991. Displacements, segment linkage and relay ramps in normal fault zones. Journal of Structural Geology 13, 721–733.

Peacock, D.C.P., Sanderson, D.J., 1994. Geometry and development of relay ramps in normal fault systems. American Association of Petroleum Geoscientists Bulletin 78, 147–165.

Peacock, D.C.P., Zhang, X., 1993. Field examples and numerical modelling of oversteps and bends along normal faults in cross-section. Tectonophysics 234, 147–167.

Ramsay, J.G., Huber, M.I., 1987. Folds and Fractures. In: The Techniques of Modern Structural Geology, vol. 2. Academic Press Ltd, London.

Schöpfer, M.P.J., Childs, C., Walsh, J.J., 2006. Localisation of normal faults in multilayer sequences. Journal of Structural Geology 28, 816−833.

Segall, P., Pollard, D.D., 1980. Mechanics of discontinuous faults. Journal of Geophysical Research 85, 4337−4350.

Soliva, R., Benedicto, A., 2004. A linkage criterion for segmented normal faults. Journal of Structural Geology 26, 2251−2267.

Sibson, R.H., 1998. Brittle failure mode plots for compressional and extensional tectonic regimes. Journal of Structural Geology 20, 655−660.

Sibson, R.H., 2000. Fluid involvement in normal faulting. Journal of Geodynamics 29, 469−499.

Treagus, S.H., 1981. A theory of stress and strain variations in viscous layers, and its geological implications. Tectonophysics 72, 75−103.

Treagus, S.H., 1983. A theory of finite strain variation through contrasting layers, and its bearing on cleavage refraction. Journal of Structural Geology 5, 351−368.

Treagus, S.H., 1988. Strain refraction in layered systems. Journal of Structural Geology 10, 517−527.

Treagus, S.H., Lisle, R.J., 1997. Do principal surfaces of stress and strain always exist? Journal of Structural Geology 19, 997−1010.

Wallace, W., 1861. The laws which regulate the deposition of lead ores in veins: illustrated by an examination of the geological structure of the mining districts of Alston Moor. Stanford, London.

Walsh, J.J., Watterson, J., Bailey, W.R., Childs, C., 1999. Fault relays, bends and branch-lines. Journal of Structural Geology 21, 1019−1026.

Walsh, J.J., Bailey, W.R., Childs, C., Nicol, A., Bonson, C.G., 2003. Formation of segmented normal faults: a 3-D perspective. Journal of Structural Geology 25, 1251−1262.